Three-dimensional identification of flow-induced noise sources with a tunnel-shaped array of MEMS microphones

Yinshi Zhou, Vincent Valeau, Jacques Marchal, François Ollivier, Régis Marchiano

To cite this version:

Yinshi Zhou, Vincent Valeau, Jacques Marchal, François Ollivier, Régis Marchiano. Three-dimensional identification of flow-induced noise sources with a tunnel-shaped array of MEMS microphones. Journal of Sound and Vibration, 2020, 482, pp.115459 -. ⟨10.1016/j.jsv.2020.115459⟩. ⟨hal-03490232⟩

HAL Id: hal-03490232
https://hal.science/hal-03490232v1

Submitted on 3 Jun 2022

Three-dimensional identification of flow-induced noise sources with a tunnel-shaped array of MEMS microphones

Yinshi Zhou[a], Vincent Valeau*[a], Jacques Marchal[b], François Ollivier[b], Régis Marchiano[b]

[a] *Institut PPRIME UPR 3346, CNRS-Université de Poitiers-ENSMA, B17 - 6, rue Marcel Doré - 86022 Poitiers Cedex, France*
[b] *Sorbonne Université, CNRS, Institut Jean Le Rond d'Alembert, 4 place Jussieu, 75005 Paris, France*

Abstract

This paper deals with the development of a three-dimensional (3D) array for imaging aeroacoustic sources in the open section of an anechoic wind-tunnel, together with the associated signal processing techniques, and presents an application to the case of a wall-mounted airfoil in a flow. The 3D antenna is made of 256 digital Micro ElectroMechanical Systems (MEMS) microphones, arranged into three nearly perpendicular planar arrays enclosing the test section, the lower part of the flow being bounded by a rigid planar surface. The source under consideration is a wall-mounted NACA 0012 airfoil located in the wind-tunnel flow at a chord-based Reynolds number of 5.33×10^5 for angles of attack at 0°, 4°, 10° and 20°, generating several broadband sources of noise. A configuration with two wall-mounted airfoils in a flow using a similar large array system is also studied. The data processing is based on the beamforming technique associated to a deconvolution method (CLEAN-SC) developed in 3D and to a dipolar radiation model. The flow effects on propagation are taken into account in the beamforming technique by using the Amiet's method in terms of angle correction. The application to the airfoil demonstrates that the performances of the 3D source localization method are excellent for the wall-mounted airfoil, due to the high number of microphones and to the "tunnel" geometry allowing to surround the sources

---

*Corresponding author

Preprint submitted to Journal of Sound and Vibration *May 8, 2020*

in the flow. The different sources of noise that are to be expected are accurately identified in the third-octave bands under investigation, and are in good agreement with experimental results published in the literature. The presented results prove that a tunnel-type array including several hundreds of microphones associated to an appropriate array processing technique performs very well for studying in 3D complex aeroacoustic sources, and that cheap MEMS microphones are good candidates for measuring the sound radiation efficiently.

Keywords

3D beamforming - Aeroacoustics - MEMS microphone array - Wind-tunnel - Airfoil

1. Introduction

The aeroacoustic noise resulting from the impingement of a flow on a rigid body is encountered widely in engineering domains, such as aeronautics, ground transport and wind turbines whereas it is not a positive effect and should be reduced. For example, noise nuisance is of main concern for the public facing nowadays the increasing aeronautical activities, and thus more and more stringent civil aircraft noise regulations have been proposed by the International Civil Aviation Organization (ICAO) in Annex 16 to the Convention on International Civil Aviation [1]. To reduce noise emission, the noise source identification and the aeroacoustic optimization should be carried out during the conception phase of aircrafts, ground vehicles, wind turbines, *etc.* This is usually carried out in anechoic wind-tunnels by using scale models [2], albeit the vital achievements of computational aeroacoustics [3]. However, the identification of noise sources in terms of position, strength, directivity and generation mechanism still remains a challenging task because this kind of complex measurements rely highly on wind-tunnel facilities, microphone arrays (a set of arranged microphones, typically several tenths, with known spatial positions), flow measurement techniques and data processing strategies.

The standard experimental method widely used by research studies and industries for imaging noise sources is the beamforming technique with phased microphone arrays, which enables the directional scanning on an area consisting of a set of discretized grid points through an acoustic signal processing approach called *delay* & *sum* [4, 5]. The beamforming results are plotted on this scan area, which generates what is usually called a sound map. Some of its applications, most of which were conducted with planar microphone array, planar scanning area and monopole noise source propagation model assumption, can be found in experimental investigations of the aeroacoustic sources of flight and ground vehicles [2, 6, 7, 8]. Additionally, the beamforming technique can be associated with a deconvolution method such as DAMAS [9] and CLEAN-SC [10] in order to improve the spatial resolution of the sound maps.

Over the last ten years, this approach has been extended to the noise source identification in 3D areas for more efficient sound imaging. Some studies intended to perform 3D sound source imaging by using a monopolar noise source assumption and planar arrays, although the spatial resolution in the direction perpendicular to a planar array is known to be bad. Brooks and Humphreys [11] firstly demonstrated the feasibility of using planar microphone arrays with 3D beamforming and the DAMAS technique, with an application to the case of a flap in flow. It was found that a microphone array with a larger size provided a beam pattern more "focused" and less elongated. However, the computational cost of the DAMAS method in 3D applications is very high. Using the CLEAN-SC method, Sarradj [12] conducted 3D beamforming tests with a planar microphone array of 64 microphones for simulated noise sources with different depth. Although four different steering vectors were examined, none of them could provided both correct positions and strength of the noise sources. Geyer *et al.* [13] identified the noise sources on an airfoil located in the turbulent flow of an open jet wind-tunnel, using a planar array of 56 microphones. The sound maps calculated on a 3D scanning grid including the potential noise source area of nozzle exit and airfoil were obtained using the CLEAN-SC method. However, no correction of the noise source position due to the shear layer of the wind-tunnel flow was made, and the leading edge noise sources, located near the midspan of the airfoil, spread in the direction perpendicular to the airfoil.

Other studies focusing on 3D beamforming by developing non-planar arrays were also reported. Using four sub-arrays of 192 microphones mounted on the closed test section wall of a wind-tunnel, Padois *et al.* [14] identified the noise source generated by a cylinder in a flow without considering the dipolar nature of the aeolian tone [15]. It was found that the CLEAN-SC provided a better spatial resolution and less side lobes. Similarly, Dobler *et al.* [16] used a larger 3D microphone array of 576 microphones consisting of three sub-arrays for the noise source identification of a real car in a wind-tunnel. Although the sub-arrays were used to measure the acoustic data simultaneously, they were not considered as one unique array during the beamforming processing. The 3D sound maps were obtained by merging the beamforming results of each sub-array before using the CLEAN-SC method in a 3D scanning grid. Padois and Berry [17] examined the performance of four deconvolution methods including the DAMAS and CLEAN-SC methods for synthetic monopole noise sources in terms of accuracy of position and sound intensity, and their computational cost. This was accomplished by using a single or two perpendicular planar arrays for the beamforming processing in two-dimensional (2D) and 3D scanning zones. They found that the advantage of using the 3D array with the CLEAN-SC method are twofold, *i.e.*, (i) a significant performance improvement of beamforming processing in 3D scanning area; (ii) a good trade-off between less computation time and good accuracy of noise source identification.

However, the beamforming technique with monopole radiation assumption can not identify correctly sources of dipolar nature if their orientation is not nearly perpendicular to the planar array [18]. It then becomes necessary to implement another noise source model, especially for non-planar arrays, when identifying the flow-induced noise of complex geometries such as cylinders [15] or airfoils [19]. Hence, an approach where the dipolar noise source model was adapted for 3D beamforming algorithms, *i.e.*, conventional beamforming and multiplicative cross-spectral beamforming and the CLEAN-SC method was proposed by Porteous *et al.* [20], for which the beamforming performances were compared for the aeroacoustic noise sources identification of a cylinder and an airfoil using a non-planar microphone array of 62 microphones. Their simulations suggested that the conventional beamforming associated to the CLEAN-SC method is the most efficient method in spite of its computational cost. However, the two perpendicular sub-arrays only enclosed partially the noise source area. Due to this array geometry and the relatively weak number of microphones, the sound maps for experimental sources remained difficult to interpret, especially concerning a finite airfoil in a wind-tunnel flow.

Despite the advantage of the traditional microphone array systems, the high cost and the complexity of such devices limit evidently the implementation of large arrays of microphone. In recent years, some efforts based on using the cheap MEMS microphones were made. It involves the work of Arnold *et al.* [21], which demonstrated the cost reduction and the data processing efficiency of a modular directional acoustic array system based on 16 hybrid-packaged MEMS silicon piezoresistive microphones installed on a printed board. The system, comparable to conventional ones, provided a higher signal to noise ratio and a larger measuring frequency range than that of a single microphone. However, extensive calibration of the system in terms of directivity and accuracy was not conducted. Furthermore, Humphreys *et al.* [22] used a planar array of 128 MEMS microphones with comparable performance to the current generation of array for the aeroacoustic radiation study of a scaled landing gear. With the design of a unique array mounting architecture to the closed test section of a wind-tunnel, the measurement system presented lower cost and complexity than the traditional directional array system.

To our knowledge, the use of the 3D beamforming technique associated to a microphone array with a very large number of microphones enclosing the wind-tunnel test section was not reported before. Therefore, the main objective of this paper is to demonstrate the effectiveness of such a massive

3D array of MEMS microphones for the identification of aeroacoustic sources in wind-tunnels. This is achieved by the identification of the noise sources of a wall-mounted airfoil yielding complex aeroacoustic noise radiation at different test conditions. The 3D beamforming results are compared with the published ones of experimental and numerical investigations. The organization of the papers is as follows. The experimental apparatus including the anechoic wind-tunnel, the test model and the microphone array are presented in Sec. II. The 3D beamforming method, the deconvolution technique CLEAN-SC and its application to simulated sources, and the modeling of the flow effects are highlighted in Sec. III. Finally, the results in terms of noise sources identification for one, and then two wall-mounted airfoils using the massive 3D array are presented in Sec. IV, followed by some concluding remarks.

2. Experimental set-up

2.1. Anechoic wind-tunnel and sound source configurations

The experiments presented in this paper were carried out in the anechoic wind-tunnel of the PPRIME Institute (Fig. 1). The flow is accelerated through a nozzle with a contraction ratio of 10, enters an anechoic room with a section outlet of (0.7×0.7) m^2, and is then sucked through a collector of dimensions (width × height) (1.00×0.87) m^2. The streamwise length of the test section is 1.44 m, and the anechoic chamber has a volume of 90 m^3 and a cutoff frequency of 200 Hz. The flow is bounded on its lower part by a plank of wood, and the dimension of the boundary layer is of the order of 10 mm at the nozzle exit. The maximum flow speed of the wind-tunnel is 60 m/s (216 km/h), and the turbulence intensity of the flow is about 1.5% at the nozzle exit. The coordinate system used for this study is represented in Fig. 1. The origin of the streamwise coordinate x is located at the nozzle exit, while the origin of the vertical coordinate z is located at the lower boundary of the flow.

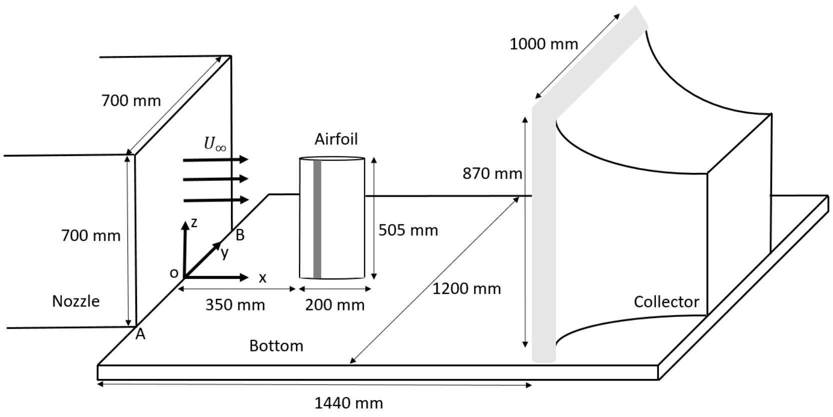

Figure 1: Diagram of the test section of the anechoic wind-tunnel, with (from left to right): the nozzle, the wall-mounted airfoil, the collector. The dark band on the airfoil stands for the boundary layer tripping device.

In order to calibrate the microphone coordinates and to evaluate the flow effects on sound propagation, a well-controlled noise source is used. It is a compression chamber emitting into a metal pipe of diameter 30 mm with two different lengths, mounted on the bottom of the test section of the wind-tunnel. The free extremity of the pipe radiates a monopole source up to a frequency of 3.3 kHz. It allows to generate a monopole noise source of broadband nature at two positions of different heights in the test section:

(0.68 m, 0 m, 0.35 m) and (0.68 m, 0 m, 0 m).

The test model generating the aeroacoustic source under study is a wall-mounted finite length NACA 0012 airfoil with a flat-ended tip and sharp trailing edge. It has a chord length $C = 200$ mm, a span length $L = 505$ mm and an aspect ratio $L/C = 2.525$. The airfoil model is mounted vertically to the bottom of the open test section, and the leading edge is located 350 mm downstream of the nozzle exit at zero-angle of attack. The NACA airfoil can be rotated around an axis located at 66.6 mm (a third of the chord length) from the leading edge; the angle of attack is then controlled by using a motorized rotating table, allowing a precision of 0.05° on the angle of attack. Special care has been taken to ensure a perfectly smooth surface of the airfoil. For all tests, the airfoil was tripped using a rough band (sandpaper) with a width of 15 mm placed at a distance of 15 mm from the leading edge along the span on one side of the airfoil surface, which allowed a forced transition of boundary layer to occur on this side and a natural transition of boundary layer to occur on the other side of the airfoil surface. The sign of the angle of attack of the finite wall-mounted airfoil is defined as positive when the tripping device is on the pressure side of the airfoil. In this paper, results are given for positive angles of attack at 0°, +4°, +10° and +20°, and a flow speed of 40 m/s, corresponding to a chord-based Reynolds number of 5.33 $\times$ 10^5. At these testing conditions, tonal noise generation is eliminated and broadband noise dominates the noise radiation, which is similar to formerly reported experimental results [23, 24, 25].

2.2. The MegaMicros system

The acoustic field is recorded by a 3D array of microphones. The development of a 3D antenna requires the use of a high number of microphones for the acoustic field to be correctly sampled and to lower spatial aliasing artifacts. Microphones dedicated to measurement are generally very reliable but they require a non versatile installation: power supply, analog/digital conversion module, many cables and in addition they are expensive. On the contrary, digital MEMS microphones embed their conditioning circuitry and analog to digital conversion stage. They require very low power supply and deliver noise free numerical signals . Consequently they provide great compactness and allow to build very versatile arrays. In addition, these microphones being used in mobile telephony are massively produced which leads to significantly low costs. As a counterpart, these microphones might be believed to provide poorer measurements. Nevertheless, Vanwynsberghe *et al.* [26] have shown that their characteristics are largely sufficient for acoustic imaging applications by using an antenna of 128 ADMP441 microphones developed by Analog Device. Indeed, these microphones are quasi-omnidirectional (1.7 dB maximum variation between -90° and + 90°). The standard deviation of their sensitivity is low (0.8 dB). The variations of the phase are acceptable because they remain lower than $\pi/20$ rad between 70 and 3000 Hz, and lower than 0.24 rad between 3000 and 10000 Hz. Finally the frequency response is not flat but since it does not vary much from one element to the other, it is known and can be corrected *a posteriori*.

The array of microphones used in this study is similar to the system described in [26], but uses 256 MEMS microphones. It is not a commercial device, and was developed at the d'Alembert Institute. The microphones are grouped by beams of 8 microphones connected to a concentrator which makes it possible to synchronize all the signals and to transfer them to a PC via a USB serial bus (see description in [26]). The beams are connected to the concentrator by a RJ45 cable. Thus each beam can be deported over large areas. For this configuration, the RJ45 cables had a length of 10 m. The beams of microphones are arranged on rigid rectilinear bars on which they are spaced regularly (every 15 cm). This mechanical constraint involves that the microphones are arranged into parallel lines of 8 regularly spaced microphones, creating a regular array.

The 3D antenna is made of three flat panels: two vertical panels (left and right-side array on Fig. 2(a)) and one quasi-horizontal panel (top-side array on Fig. 2(a)). As shown in the picture of Fig. 2(b), the 3D array totally encloses the 3/4 open test section of the wind-tunnel. These panels are placed in such a way that they form a rectangular base cone of size (width × height) about 1.2 m × 1.0 m near the air inlet and 2.0 m × 1.2 m near the outlet. The 32 beams are positioned horizontally in the direction of the flow, and each of them is fixed on one of the three panels (beams 0 to 10 on left-side array, beams 11 to 20 on the top-side and beams 21 to 31 on the right-side array). The gap between two neighbouring beams is 10 cm (except for beams 11-12 and 19-20 for which the gap is 15 cm). In this way, the acoustic field measured by the three panels is mostly meshed with rectangles of dimension 10 cm (streamwise direction) × 15 cm (spanwise direction).

The measurement by hand of the 3D positions of 256 microphones is impractical for the array geometry used in this study. For this reason, the microphones coordinates are assessed by two methods. First we used the blind alignment method developed by Ono *et al.* [27]. Later on the microphone relative positions were verified using the robust method developed by Vanwynsberghe *et al.* [28]. More exactly, these methods provide the relative positions between the 256 microphones. To obtain the absolute positions of the microphones in the coordinate system associated with the wind-tunnel (Fig. 1), the calibration process should be completed by using a reference noise source with known position. By using the 3D beamforming results associated to a monopolar radiation assumption (the algorithm will be presented in Section 3.1), and applying it to the case of the artificial monopolar noise source at position (0.68 m, 0 m, 0.35 m) with no flow, the estimated position was compared to the actual position of the source. The absolute coordinates of the 256 microphones were then obtained by subtracting to their coordinates the position errors in x, y and z-directions.

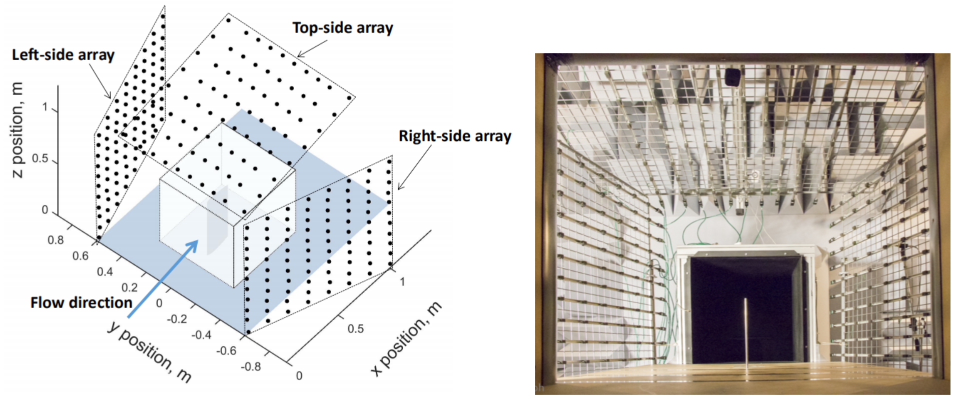

(a) (b)

Figure 2: (a) Schematic depicting the 3D microphone array and the wall-mounted airfoil. The black points indicate the positions of the microphones of the 3D microphone array. The cube with dashed edges enclosed by the 3D microphone array shows the 3D scanning grid for the beamforming calculation in a volume of dimension 0.6 m × 0.6 m × 0.6 m. (b) Picture of the experimental setup, taken from the collector of the wind-tunnel. The NACA airfoil and the collector appear at the center of the picture, and the three sub-arrays are on the top, left and right sides of the picture.

Fig. 3 shows the far-field spectra of the wall-mounted airfoil measured by a MEMS microphone and a measurement microphone (type GRAS 40F mounted with a Preamplifier 26AK) with a flat frequency response up to frequency 10 kHz, at the same location. The spectrum of the GRAS microphone is taken as a reference result. The considered case is the noise radiated by the airfoil at angle of attack 10° and flow speed 40 m/s. As expected, the noise radiated by the airfoil is of broadband nature, with no tonal components. The energy content decreases with frequency, with a sudden drop around frequency 3.5 kHz that could be attributed to a wind-tunnel effect. A similar spectral behaviour was observed by Moreau *et al.* for a wall-mounted NACA 0012 airfoil at 35 m/s [19].

Some differences are observed in terms of spectra between the reference and the MEMS microphone, especially at high frequencies. It indicates a trend of the MEMS microphones to overestimate the noise level, from around 1 dB at 300 Hz, increasing up to around 5 dB at 3 kHz. The overestimation drops down around 3.5 kHz, and increases again up to 8-10 dB for frequencies higher that 5 kHz. Such differences were already reported in [26], based on a sample of 128 microphones. With a high number of microphones, it is not possible to perform an individual amplitude calibration for each microphone. However, it is possible to perform some frequency equalization with the mean frequency response of the MEMS microphones. In this study, such a frequency equalization was carried out, using the frequency variation of the average sensitivity obtained from the test of a set of microphones (model ADMP441) by Vanwynsberghe *et al.* [26]. This will allow the levels in dB ref. 2.10^{-5} Pa, that are given in different octave bands, to be compared to each other.

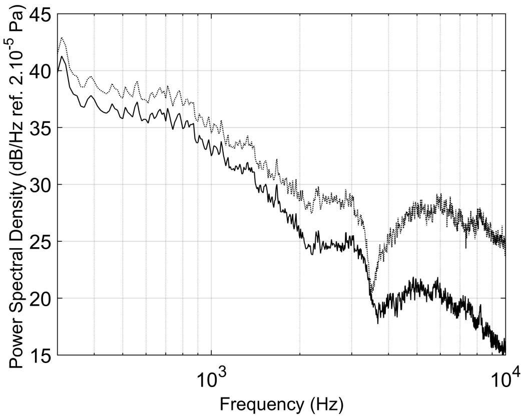

Figure 3: Comparison of the far-field acoustic power spectral density for the wall-mounted finite airfoil at velocity $U = 40$ m/s for angle of attack $\alpha = 10^\circ$ using a MEMS microphone (dotted line) and a GRAS microphone (plain line).

3. Array processing technique

3.1. Three-dimensional beamforming

Processing techniques. The beamforming method used in this study is based on the *delay* & *sum* process. Consider an array of M microphones (described by their position $\boldsymbol{x_m}$, with $1 \leq m \leq M$) located in the pressure far-field generated by noise sources. A scanning domain, that is a plane (generally parallel to a planar array) for 2D beamforming or a volume for 3D beamforming, is chosen to enclose the potential noise sources. During the beamforming process, it is discretized and represented by a scanning grid (described by the position $\boldsymbol{x_f}$). For each point $\boldsymbol{x_f}$, the "beamformed signal" in the frequency domain is given by the following equation:

$$Z(\boldsymbol{x_f}, \omega) = 1/M \sum_{m=1}^{M} P(\boldsymbol{x_m}, \omega) e^*(\boldsymbol{x_m}, \boldsymbol{x_f}, \omega), \tag{1}$$

where $\omega = 2\pi f$ is the angular frequency, $P(\boldsymbol{x_m}, \omega)$ the Fourier transform of the far-field pressure signals recorded by the mth microphone, the symbol * the complex conjugate operator, and $e(\boldsymbol{x_m}, \boldsymbol{x_f}, \omega)$ the steering function. This steering function describes the propagation between $\boldsymbol{x_m}$ and $\boldsymbol{x_f}$, and is dependent on the assumption that is made on the source radiation: most generally, a monopolar radiation is considered.

Using the vector notation $\boldsymbol{P} = (P(\boldsymbol{x_1}, \omega)...P(\boldsymbol{x_M}, \omega))^T$ and $\boldsymbol{e} = (e(\boldsymbol{x_1}, \boldsymbol{x_f}, \omega)...e(\boldsymbol{x_M}, \boldsymbol{x_f}, \omega))^T$ with the symbol ^{T} indicating the transpose operator, the frequency-domain beamforming function at each scanning point $\boldsymbol{x_f}$ is given by:

$$A(\boldsymbol{x_f}, \omega) = Z(\boldsymbol{x_f}, \omega) Z(\boldsymbol{x_f}, \omega)^H = \frac{\boldsymbol{e}^H \boldsymbol{C} \boldsymbol{e}}{\|\boldsymbol{e}\|^4}, \tag{2}$$

where the Cross Spectral Matrix (CSM) of size $(M \times M)$ is defined as $\boldsymbol{C} = \boldsymbol{P}\boldsymbol{P}^H$, ^{H} being the Hermitian transpose operator. The CSM is a Hermitian matrix $(C_{ij}(\omega) = C^*_{ji}(\omega))$.

The steering vector $\boldsymbol{e}$ enables the microphone array to "steer" to different scanning points $\boldsymbol{x_f}$. Most generally, a monopolar assumption is used, and the elements e of the corresponding steering vector can be written:

$$e(\boldsymbol{x_m}, \boldsymbol{x_f}, \omega) = exp(-j\omega r_m / c_0), \tag{3}$$

where $r_m = |\boldsymbol{x_m} - \boldsymbol{x_f}|$ and c_0 is the speed of sound. In this case, the term $\|\boldsymbol{e}\|^4$ is equal to M^2. In the case of a quiescent medium, the time delay $\tau(\boldsymbol{x_m}, \boldsymbol{x_f})$ can be simply given by r_m/c_0. When the influence of flow on propagation is significant such as in a wind-tunnel, methods based on ray tracing [29, 30] could be used to calculate the steering vector. The way that the flow effect on propagation is taken into account in this study is presented in Section 3.3.

For 3D beamforming, the monopolar noise source assumption is usually not appropriate, because aeroacoustic noise sources induced by the interaction of a solid body tend to have a radiation that can be approximated by a dipolar radiation [31]. The steering function for a point dipole source in the beamforming technique can be written by introducing a correction term to the monopolar steering vector of Eq. (3) according to [20]:

$$e_d(\boldsymbol{x_m}, \boldsymbol{x_f}, \omega) = e(\boldsymbol{x_m}, \boldsymbol{x_f}, \omega) \left(\boldsymbol{\xi} \cdot \frac{\boldsymbol{x_m} - \boldsymbol{x_f}}{r_m} \right), \tag{4}$$

where $\boldsymbol{\xi}$ is the orientation of the dipole source. The advantage of using such a steering vector is that the frequency-domain beamforming function exhibits a maximum at the source location for a dipolar source, so that the sound maps can be readily interpreted. However, Eq. (4) shows that an assumption on the dipole orientation $\boldsymbol{\xi}$ is required. In the present case, the wall-mounted airfoil has a symmetric section of NACA 0012 profile, for which the orientation of the dipole is known to be perpendicular to the airfoil surface.

The matrix $\boldsymbol{A}$ calculated for a given frequency is a $(N \times N)$ matrix in 2D domain, or a $(N \times N \times N)$ matrix for the 3D domain. N is the grid point number per dimension. The elements of $\boldsymbol{A}$ are real and positive by definition. The so-called sound map is produced by plotting the matrix $\boldsymbol{A}$ for a given frequency with respect to the coordinates of the grid points.

To obtain sound maps with a satisfactory dynamical range, the so-called trimmed version of the CSM is used in this study (the diagonal elements of the CSM being set to zero), in order to remove the contribution of the noise induced by the interaction of the wind with the microphones [5]. Indeed in this study the array is located out of the flow, but close enough to the test section, so that hydrodynamic pressure perturbations could be expected due to flow re-circulation at low velocity.

Deconvolution. The sound map obtained by beamforming is the result of the convolution of the sound source distribution with the array response to a point source (monopole or dipole) with the corresponding radiation model. The sound map calculated using beamforming consists of a main lobe centered on the source position and of side lobes. As a result, the sound source imaging of the beamforming technique can only provide approximately the source location and its distribution for the reason that the size of the lobes are frequency-dependent and the side lobes can be identified as sound sources. In order to improve the spatial resolution and to make the sound maps more readily interpretable, the so-called deconvolution methods, which deconvolve the array response from the beamforming maps, can be associated to the beamforming algorithm. The advantage are twofold: (i) the side lobes are removed from sound maps; (ii) a good resolution of source distribution can be achieved in all frequency bands.

The DAMAS method (Brooks *et al.* [9]) is based on Point Spread Functions (discussed in the next section) for which the noise source at each scanning grid is supposed to be a point monopole source with uniform radiation pattern. This technique is computationally expensive because in 3D applications, the number of equations to solve is of the order of N^3 (N being the number of scanning points per dimension). In contrast, the CLEAN-SC method (Sijtsma [10]) is less demanding as it searches the peaks of the sound map at each iteration, and an adaptation of this technique to 3D applications, using monopolar and dipolar radiation models, is used in this paper. The method is similar to the one developed by Porteous *et al.* [20].

The CLEAN-SC technique works as follows: by finding the peak level in the sound map of beamforming results (or "dirty map" for the CLEAN-SC method), this method allows to determine the main lobe, its values and its coherent source spots including its side lobes. A portion of their amplitude, determined by a safety factor in this approach, are then removed from the "dirty map". This process is done iteratively with a stop criterion. All the main lobes identified in the process are replaced by so-called clean beams with a predefined beamwidth. A sound map called "clean map" with better spatial resolution is finally obtained. In this paper, the 3D sound maps obtained by using the CLEAN-SC technique contain only clean beams.

The CLEAN-SC method is not efficient for the identification of noise sources that are spatially close, overlapping and forming a single peak level in sound maps. This problem usually arises at low frequencies. In addition, a source area containing coherent noise sources limits the application of the CLEAN-SC method (Bahr and Cattafesta [32]). However, this method has been demonstrated to provide a good compromise between computation cost and efficiency [20, 17].

3.2. Numerical simulations

Some simulations were conducted by using synthetic white noise sources (monopole, dipole and distributed dipole noise sources). The actual 3D array geometry used in the wind-tunnel measurements is used in these simulations. The aim is to carry out a first evaluation of the 3D array performance, and to introduce the corresponding notions of 3D sound maps for dipole noise sources.

Three-dimensional Point Spread Function. The sound map showing the beamforming results for a point monopole source is generally called the point spread function (PSF). Fig. 4 yields the simulated 3D PSF at frequencies 1 kHz, 2 kHz and 4 kHz of a broadband point monopole noise source located at position (0.5 m, 0 m, 0.5 m), using the experimental 3D array geometry of Fig. 2(b). Similarly to 2D beamforming results, a main lobe shown by the isosurfaces of ellipsoid shape centered on the noise source position is observed, together with side lobes evidenced by isosurfaces with lower level. At higher frequencies, the side lobes appear periodically in the y-direction, pointing out the need for an efficient deconvolution technique. The presence of such lobes is due to the the structure of the array, in particular the two parallel vertical arrays facing each other.

The resolution is generally defined as the beamwidth of the main lobe of the PSF at a value of 3 dB below the peak level for 2D beamforming, and gives an order of magnitude of the minimum distance between two sources for being discriminated. In 3D cases associated with the 3D array geometry in the study, the isosurface below 3 dB of the peak level is an ellipsoid. In order to estimate its size, an average of the three major principle axis of the ellipsoid was computed for each case from the results of Fig. 4. This value for the 3D sound maps of 1 kHz, 2 kHz and 4 kHz is respectively 176 mm, 88 mm and 43 mm (obtained by a 3D scanning grid with spatial resolution of 2 mm), from which an inverse proportionality between the size of the ellipsoid and the beamforming frequency is expected; the results show indeed that the beamwidth at -3 dB is very close to half-a-wavelength. This result was explained by Cassereau *et al.* [33] in the ultrasound domain. The major principal axis of the ellipsoid is nearly in the x-direction to which no sub-array is perpendicular, which yields a lower spatial resolution in this direction; practically, this direction is the streamwise direction, as no microphone can be located in the flow. Logically, the results show that the size of the main and side lobes decreases at increasing frequency, allowing a better spatial resolution in the medium frequency range ([2 kHz; 4 kHz]).

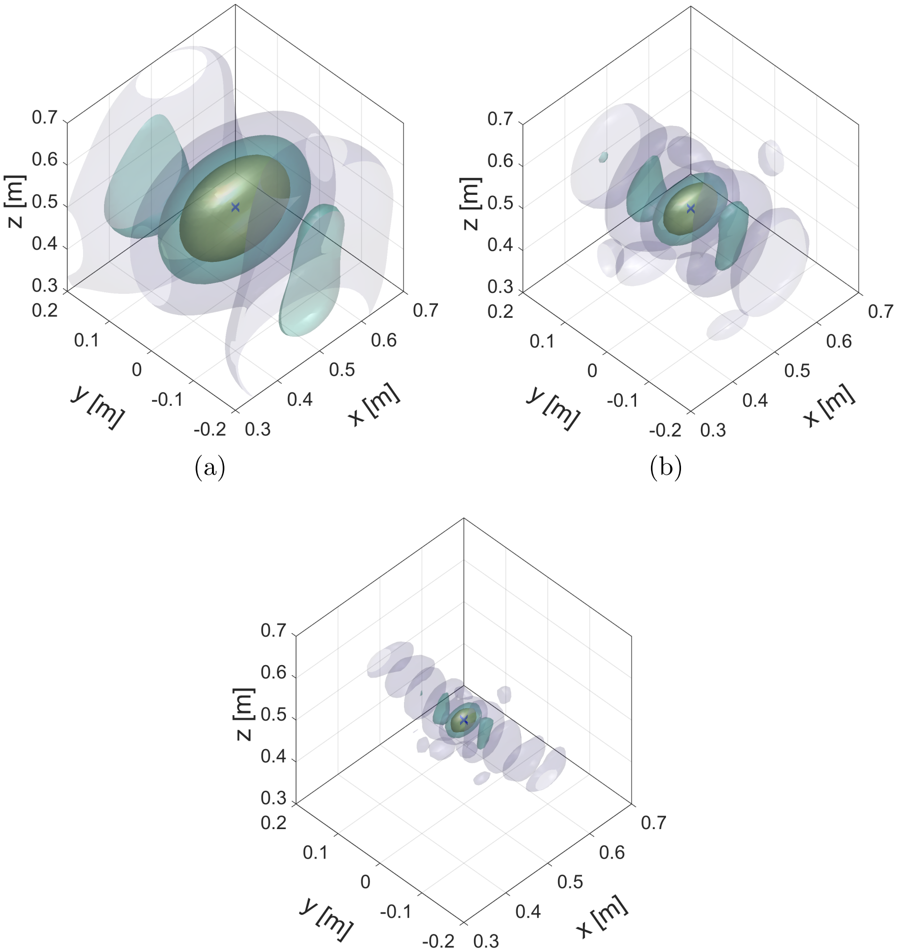

(a) (b) (c)

Figure 4: Sound maps of a synthetic monopole noise source at the position (0.5 m, 0 m, 0.5 m) showing 3D point spread function at frequency (a) 1 kHz, (b) 2 kHz, (c) 4 kHz. The 3D isosurfaces at 3 dB, 6 dB and 12 dB below the peak level are plotted in each sound map from the inside to the outside. The symbols '×' denote the exact location of simulated monopole noise source.

Results for a point dipole source. Fig. 5 shows the 3D beamforming results for a simulated broadband dipolar source, located at (0.5 m, 0 m, 0.5 m), and oriented along the y-direction using different steering vectors. Fig. 5(a) shows the sound map obtained using a monopolar steering vector at an analysis frequency of 3 kHz. Two dominant lobes are observed near the real source position. Indeed, it yields the existence of a dipole source (Liu *et al.* [18]) whereas its exact location is ambiguous: the lobes are in fact two out-of phase monopoles creating the dipolar radiation. Fig. 5(b) shows the sound map obtained using a dipolar steering vector, correctly oriented by setting $\boldsymbol{\xi} = (0,\ 1,\ 0)$ (Eq. 4). In spite of two side lobes near the noise source position, the dipole is clearly identified by the main lobe with a maximum coinciding exactly with the simulated dipole location with comparison to Fig. 5(a). The result of searching for a dipole with incorrect orientation $\boldsymbol{\xi} = (1,\ 0,\ 0)$ (perpendicular to the real orientation) is shown in Fig. 5(c). In this case four main lobes appear around the source location. Knowing that incorrect orientation can lead to an incorrect sound map, one disadvantage of beamforming using a dipolar steering vector is that the orientation of dipole should be assessed priorly.

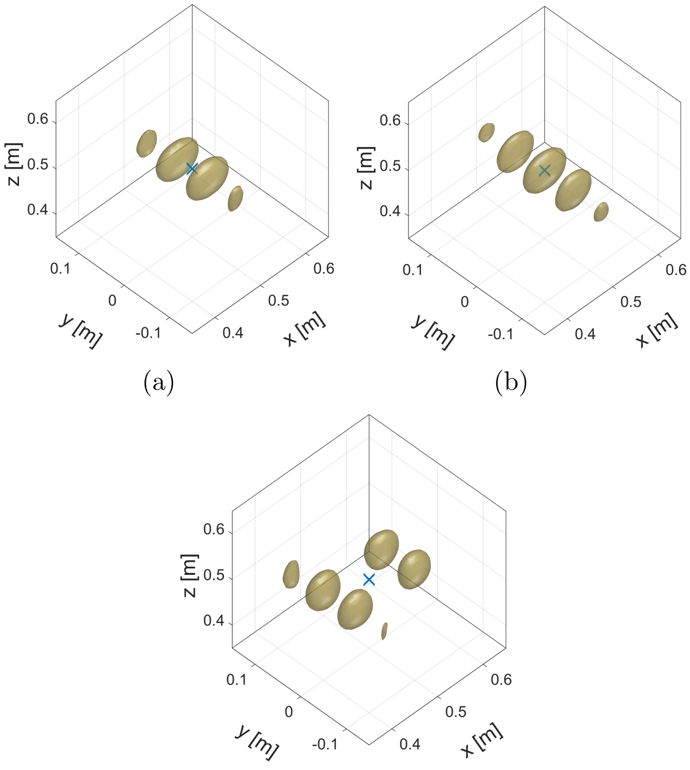

(a)

(b)

(c)

Figure 5: Sound maps at beamforming frequency $f = 3$ kHz of a synthetic dipole noise source at the position (0.5 m, 0 m, 0.5 m) , (a) using a monopole steering vector, (b) using a dipole steering vector with $\boldsymbol{\xi} = (0,\ 1,\ 0)$, (c) using a dipole steering vector with wrong orientation of the dipole $\boldsymbol{\xi} = (1,\ 0,\ 0)$. The symbols '×' denote the exact location of simulated dipole noise source. The 3D isosurface in each sound map is plotted at 3 dB below the maximum.

Results for distributed dipole sources. Real aeroacoustic sources may have a spatial extent and can be distributed spatially, depending on the geometric characteristics of the object radiating sound. A typical example is the application case of this paper: for the wall-mounted airfoil, the trailing edge noise source can be distributed along the span of the airfoil. In order to evaluate the CLEAN-SC method for this type of noise source, 11 incoherent dipole noise sources of broadband nature with orientation $\boldsymbol{\xi} = (0, 1, 0)$ and same intensity were simulated on a line in the z-direction; the objective of such a model is to simulate a continuous distribution of broadband dipolar sources, evenly distributed along a vertical line of 0.5 m, approximately equal to the airfoil's span. In this purpose, the distance between two neighbouring sources is 5 cm. The experimental 3D array geometry is used in the simulation, and the sound maps in Fig. 6 are plotted in a third-octave band [2245 Hz; 2828 Hz] of nominal midband frequency of 2.5 kHz. Fig. 6(a) shows that the main and side lobes are distributed evenly in the z-direction because the distance between the neighbouring sources is too small for discriminating the individual dipoles. Indeed the investigation of the PSF indicated a resolution of about half-a-wavelength, and the distance between the sources (5 cm) is here less than the half-a-wavelength. In addition, the position of the main lobe is ambiguous through the observation of the size of the lobes on the sound map. Fig. 6(b) shows the sound map after deconvolution, from which a continuous distribution of noise sources is revealed, exactly located along the linear segment where the sources were generated. The side lobes are perfectly removed after deconvolution. It is concluded that the 3D version of the CLEAN-SC method used in this study is efficient to locate in the 3D space a continuous distribution of dipoles in the mid-frequency range (*i.e.*, frequencies of the order of a few kHz).

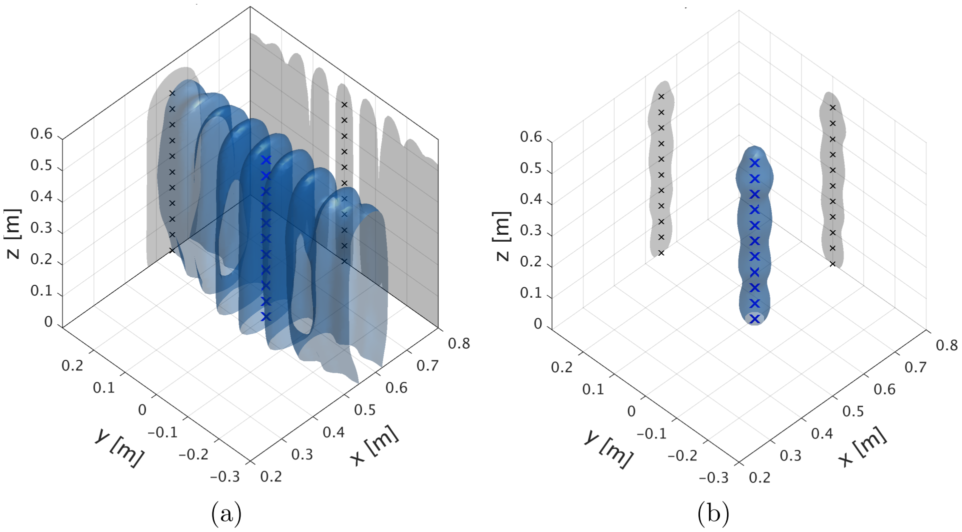

Figure 6: Sound maps for a distributed noise sources of 11 synthetic dipoles at a third-octave band of nominal midband frequency of 2.5 kHz. (a): 3D dipolar beamforming; (b): CLEAN-SC technique. The symbols '×' denote the exact location of simulated dipole sources. The shadows and the small black symbols '×' correspond respectively to the projection of the 3D sound source imaging and the real noise source position in different directions. The 3D isosurface in each sound map is plotted at 9 dB below the maximum.

3.3. Modeling of the flow effects on sound propagation

The beamforming technique is based on a propagation model from a sound source to a microphone. The most straightforward way of implementing the beamforming technique is to use a model based on the Green function in a quiescent medium. However, in the present application, the sound source is located in a flow while the array is outside the flow, so that the wavefronts undergo convection and refraction effects. If the flow effect is not properly taken into account by using appropriate "flow effect corrections", the beamforming output produces an apparent shift of the source, upstream the actual position of the source [34, 35].

In this study, such effects have been assessed experimentally by using the artificial monopolar noise source presented in Section 2.1. The 3D sound maps were produced by using a monopolar steering vector; the clean beamwidth for the CLEAN-SC technique is set to 0.05 m, and the safety factor is set to 0.99. The position with maximum level of the 3D beamforming sound map was considered to be the estimated position of the monopolar source. A 3D scanning grid with a spatial resolution of 5 mm was set for the 3D beamforming concerning the two test cases in this section.

A sample example is given in Fig. 7, which shows the 3D beamforming results without flow effect correction (Green function with a quiescent medium assumption) concerning the monopolar noise source embedded in the floor of the wind-tunnel at flow speed 40 m/s and position (0.68 m, 0 m, 0 m). First, it is observed that the raw beamforming sound map (Fig. 7(a) is difficult to interpret due to the presence of ambiguous side lobes, while the use of the CLEAN-SC deconvolution technique allows the unambiguous identification of a source located at $z = 0$ m (Fig. 7(d)). However, as expected, the estimated position is significantly shifted downstream the actual position (6.5 cm in this case). This apparent spatial shift in the streamwise direction x is noted down Δx_{3D} in Fig. 7(d). Let us specify here that the number of iterations using the CLEAN-SC method is 16 in the present case, and that only the corresponding clean beam is represented in the sound map of Fig. 7(d). It means that 16 sources were identified before reaching the stop criterion. It can be observed that the peak level of the "dirty map" in Fig. 7(b), obtained after removing the main lobe identified at the first iteration and its coherent side lobes, is 20 dB lower than that of Fig. 7(a). Fig. 7(c) shows that the peak level of the “dirty map” after 2 iterations is 26.3 dB, indicating a much lower background noise level with respect to the synthetic noise source.

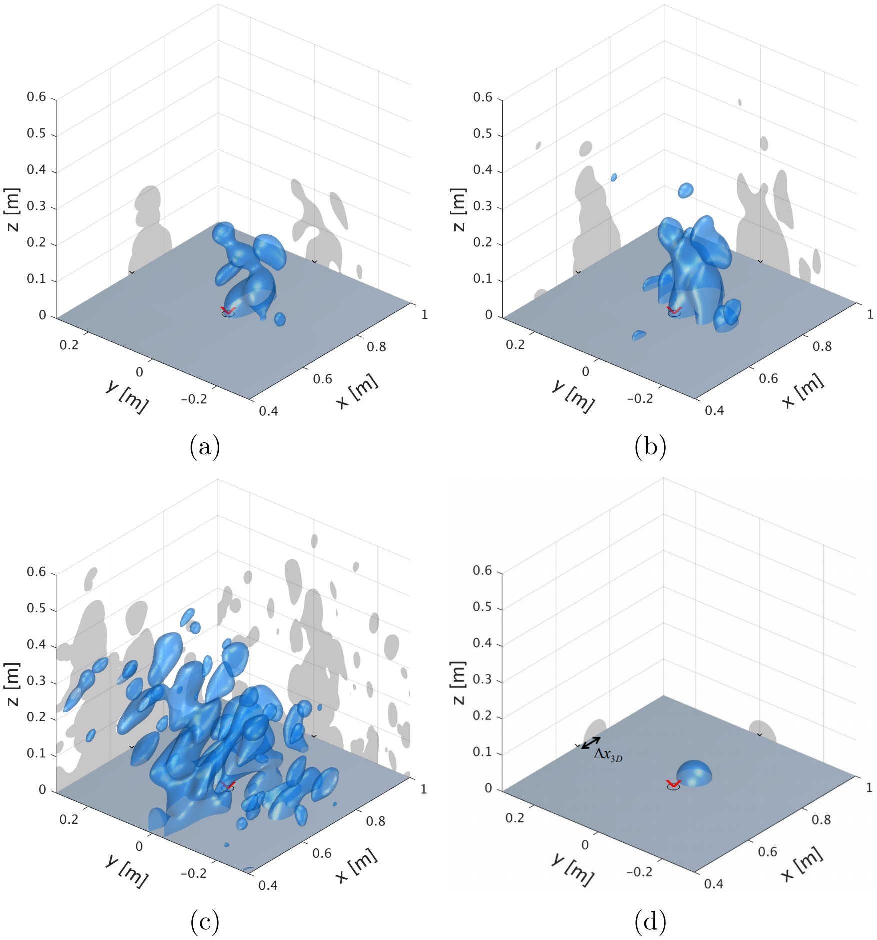

(a) (b) (c) (d)

Figure 7: Sound maps without flow effect correction at frequency 3 kHz of the synthetic noise source at (0.68 m, 0 m, 0 m) generated by a compression chamber at an incoming velocity $U_\infty = 40$ m/s in the wind-tunnel. (a): 3D monopole beamforming with a peak level at 51.3 dB; (b): 3D "dirty map" after the first iteration with a peak level at 31.3 dB; (c): 3D "dirty map" after the second iteration with a peak level at 26.3 dB; (d): CLEAN-SC technique with maximum value of 51.3 dB on the sound map. The red symbols '×' denote the exact location of synthetic monopole noise source. The black circles indicate the metal pipe position. The shadows and the black symbols '×' correspond respectively to the projection of the 3D sound source imaging and the real noise source position in different directions. The 3D isosurface in the sound maps is plotted at 9 dB below the maximum.

The Amiet's model [29] is a well-known model for taking into account the refraction and convection effects of flow on sound propagation. It is based on a ray-tracing approach and on the assumption that the shear layers are infinitely thin. In this paper, an implementation of the Amiet's method in three dimensions is used, following the equations derived by Bahr *et al.* [36]. In the present work, the shear layers are modeled according to three planar and infinitely thin shear layers, as depicted in Fig. 8, and only the angle correction is addressed. To illustrate the interest of the Amiet's method, a noise source is supposed to be at the position (x_0, y_0, z_0). Three microphones were considered around the shear layers of the wind-tunnel. The ray paths from the noise source to the three microphones were computed at a wind speed of 40 m/s. Fig. 8 shows that the calculated ray paths (intersecting with the shear layers at point I) are not straight from the noise source to the microphones, which involves a modification of the propagation time from the source to the microphone, compared to a rectilinear path.

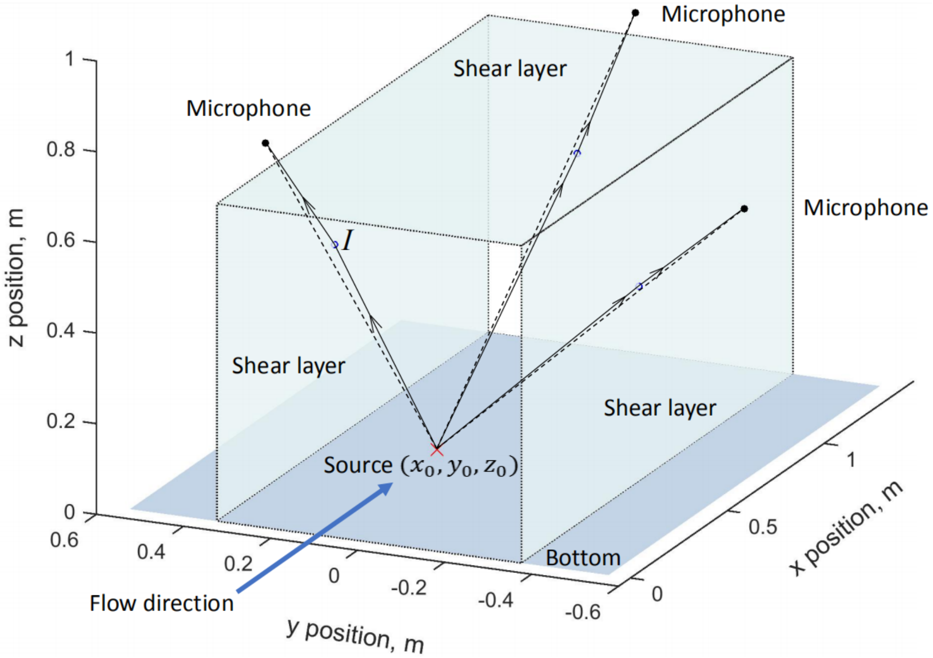

Figure 8: Sketch of the sound rays in the wind-tunnel flow. The calculated sound rays from the noise source to the microphones are indicated by solid black lines, while the rectilinear paths are depicted by dashed lines.

An evaluation of the implemented “flow effect correction” technique is now considered, for an experimental case using the artificial noise source at height $z = 0.35$ m and for a flow speed of 40 m/s. Fig. 9 shows the 3D sound beamforming sound maps of this test case. Without flow effect correction, Fig. 9(a) shows that the main lobe of the sound map is not centered at the free end of the metal pipe as expected. Similar to Fig. 7(d), the sound map after deconvolution reveals clearly the shift downstream (6 cm in this case) of the noise source with respect to the expected position shown by the red cross (see Fig. 9(b)). Note that the apparent shift Δx_{3D} of the noise source due to the flow effect is not the same at different heights in the test section.

According to Fig. 9(c) with flow effect correction, the contribution of the aeroacoustic sources of the cylinder seems to be weak at the beamforming frequency. In addition, the merging of a main lobe and of some side lobes at the top area of the pipe makes it difficult to identify the real noise source. By using the 3D CLEAN-SC code, the noise source is well located at the top of the pipe (Fig. 9(d)). The position error of noise source in 3D sound map is less than 8 mm. It is then concluded that the 3D microphone array provides good performances in terms of noise source position accuracy for isolated noise sources, and that the modeling of the flow effects on propagation is satisfactory, as the source apparent shift (previously observed in Fig. 7(d)) is not present anymore.

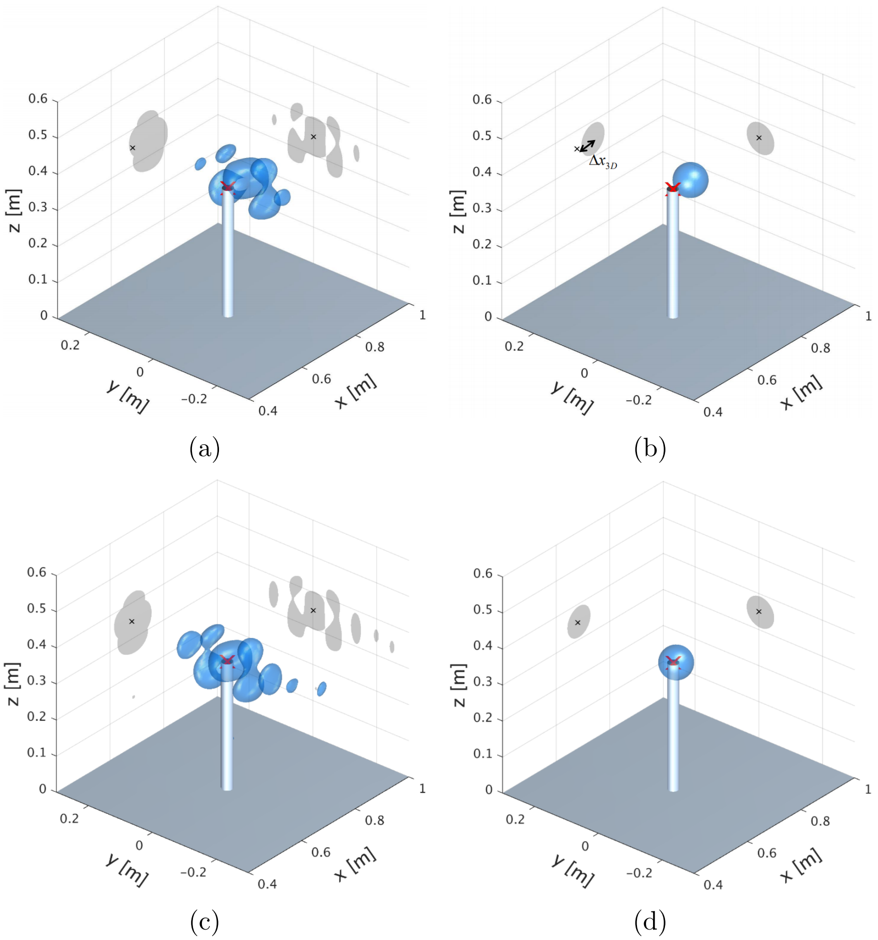

(a) (b)

(c) (d)

Figure 9: Sound maps at frequency 3 kHz of the synthetic noise source at (0.68 m, 0 m, 0.35 m) generated by a compression chamber at an incoming velocity $U_\infty = 40$ m/s in the wind-tunnel. (a): 3D dipolar beamforming without flow effect correction with maximum value of 52.2 dB on the sound map; (b): CLEAN-SC technique without flow effect correction with maximum value of 52.2 dB on the sound map; (c): 3D dipolar beamforming with flow effect correction with maximum value of 52.2 dB on the sound map; (d): CLEAN-SC technique with flow effect correction with maximum value of 52.2 dB on the sound map. The red symbols '×' denote the exact location of synthetic monopole noise source. The white cylinder represents the pipe connected to the compression chamber. The shadows and the black symbols '×' correspond respectively to the projection of the 3D sound source imaging and the real noise source position in different directions. The 3D isosurface in each sound map is plotted at 9 dB below the maximum value of the sound map.

4. Results and discussion

4.1. Three-dimensional dipolar beamforming implementation

Acoustic data from the 256 channels were recorded at a sampling frequency of 50 kHz with a sampling time of 5 s for each test case. During the array signal processing, the signal of each channel was filtered by a 256^{th} order numerical high-pass filter with a cutoff frequency of 20 Hz. The CSM was obtained by using the Welch's method, for which each channel data set was divided into 100 blocks containing 2500 sampling points without overlap and a Hanning window. The resulting frequency resolution was 20 Hz, and the computed CSM for 3D beamforming was then a matrix of dimension (256×256×2500), 256 being the number of microphones and 2500 the number of discrete frequency values. A 3D scanning grid containing 226981 points (61^3) in a cube of dimension 0.6 m × 0.6 m × 0.6 m enclosing the wall-mounted airfoil, was used for all the sound maps in this section (Fig. 2(a)). The grid was then composed of cubes with an edge length of 10 mm. The safety factor of the CLEAN-SC method was set to 0.99 and the clean beamwidth was chosen as 0.05 m [10]. The dipolar nature of the trailing edge noise [19] and leading edge noise sources [37] was taken into consideration by making the assumption that the dipole orientation is perpendicular to the airfoil symmetry axis.

Beamforming results are given in third-octave bands in the following. This was achieved by calculating the beamforming sound maps for each frequency bin contained in a given third-octave band, and then summing the

3D sound maps. Four third-octave bands are considered in this study, *i.e.*, [707 Hz; 891 Hz], [2245 Hz; 2828 Hz], [3564 Hz; 4490 Hz] and [4490 Hz; 5657 Hz], with respective nominal midband frequencies of 0.8, 2.5, 4 and 5 kHz.

4.2. Sound source localization results for a wall-mounted airfoil

As mentioned in Section 2.1, this paper focuses on the sources of broadband noise produced by a wall-mounted airfoil in a flow. Several noise sources, including trailing edge noise and wing tip noise (Brooks *et al.* [38]), leading edge noise (Geyer *et al.* [13]) and junction noise (Moreau *et al.* [39]), are expected to be observed in the 3D sound maps. In all the sound maps presented in this section, the 3D isosurface at 9 dB below the maximum is systematically plotted in order to investigate the spatial distribution of the aeroacoustic sources. Figs. 10, 11 and 12 present the 3D sound maps at incoming flow speed 40 m/s, for midband frequencies of 2.5 and 4 kHz, at increasing angles of attack (4°, 10° and 20°). At the end of the section, the case $\alpha = 0°$ is presented to discuss the results at lower and higher midband frequencies (0.8 and 5 kHz, Fig. 13).

Figs. 10(a) and 10(c) present the results at angle of attack $\alpha = 4°$ using the 3D beamforming technique, for two third-octave bands with respective midband frequency 2.5 and 4 kHz. At frequency 2.5 kHz, one lobe at the corner of the junction and the leading edge can be observed in Fig. 10(a), which may correspond to dipolar leading edge noise generated by the impingement of the wall turbulent boundary layer on the leading edge [37, 39]. At both frequencies, some larger vertical lobes parallel to the airfoil appear, located regularly between the two vertical sub-arrays (Figs. 10(a) and 10(c)). The lobe with maximum intensity is centered on the trailing edge and may be interpreted as the main lobe of the dipolar source of trailing edge noise. The other lobes, parallel to the main lobe, do not coincide with a solid boundary located in the flow, and should be interpreted as side lobes. The observed network of parallel vertical lobes is similar to the map in Fig. 6(a) reporting the simulation of a vertical linear distribution of dipolar sources. The comparison between Figs. 10(a) (2.5 kHz) and 10(c) (4 kHz) also indicates that at increasing frequency, the spatial extent of the main and side lobes diminishes, providing a better resolution, which is similar to 2D beamforming.

Using the deconvolution method CLEAN-SC, an easily interpretable sound map is obtained thanks to the side lobes removal, as shown in Figs. 10(b) and 10(d). It is found that the noise source is distributed rather evenly along the trailing edge for both frequency bands. These results are, again, similar to the simulation results of Fig. 6(b). Therefore, it is concluded that the CLEAN-SC model, based on a superimposition of incoherent sources, is valid for describing the broadband trailing edge noise source. These results are in agreement with the literature. A similar noise source distribution of a tripped wall-mounted NACA 0012 airfoil identified by two-dimensional beamforming method was reported before in the same frequency range (Moreau *et al.* [39]; Geyer *et al.* [40]), with an elongated source evenly distributed along the trailing edge. In addition, at higher frequency (4 kHz), the apparent diameter of the line source along the trailing edge slightly increases close to the tip (Fig. 10(d)), which means that the intensity of the source is higher at the tip. Moreau *et al.* [39], similarly, reported on a similar tripped NACA 0012 airfoil at angle of attack 4° (with a similar length/chord ratio $L/C = 3$, but at a higher flow speed of 60 m/s) the apparition of tip noise around 4 kHz, but also that trailing edge noise almost disappears at this frequency.

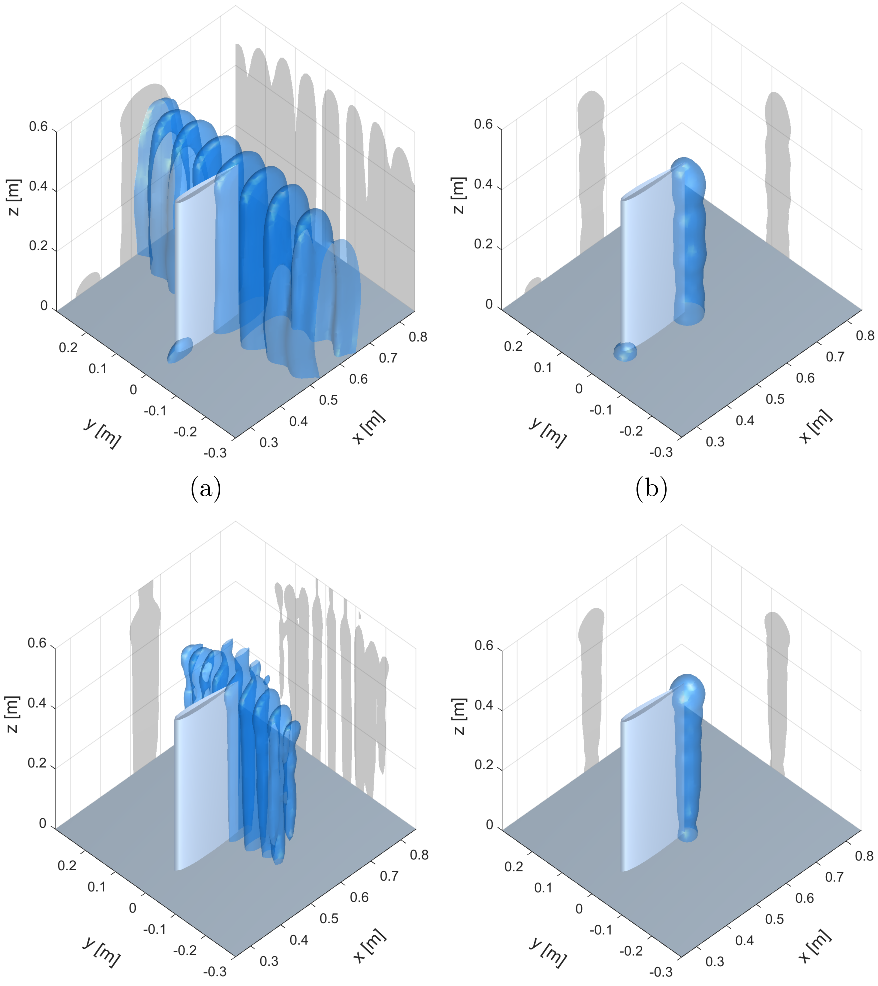

(a) (b)

(c) (d)

Figure 10: Sound maps for the wall-mounted finite airfoil at incoming velocity $U_\infty = 40$ m/s and angle of attack $\alpha = 4°$, at two third-octave bands of nominal midband frequency 2.5 kHz (top figures) and 4 kHz (bottom figures). (a) and (c): 3D dipolar beamforming with respectively a maximum value of 35.7 dB and 29.8 dB on the sound map; (b) and (d): CLEAN-SC technique with respectively a maximum value of 33.1 dB and 29.8 dB on the sound map. The 3D isosurface in each sound map is plotted at 9 dB below the maximum value of the sound map.

Fig. 11 presents the sound maps of the wall-mounted airfoil at angle of attack $\alpha = 10°$ and flow speed 40 m/s. As shown in Figs. 11(a) and 11(c), the beamforming results without deconvolution make difficult the interpretation of the noise sources, due to the presence of strong side lobes. Again, the use of the 3D CLEAN-SC method reveals the sound source distribution (Figs. 11(b) and 11(d)). The sound map at frequency 2.5 kHz (Fig. 11(b)) is quite similar to the one at angle of attack $\alpha = 4^\circ$ at the same frequency (Fig. 10(b)), except that the noise sources are less evenly distributed along the trailing edge. Indeed, it consists of three different parts in the spanwise direction, *i.e.*, a concentrated noise source located at the corner of the trailing edge and the wing tip (tip noise), a distributed noise source in the middle span of the airfoil (trailing edge noise), and a concentrated noise source identified at the corner of the trailing edge and the junction. Tip noise and junction noise originate from complex flow regimes in those corresponding zones, as reported by several research studies focused on the investigation of the wing tip flow (Uzun *et al.* [41], Imamura *et al.* [42], Bailey *et al.* [43]) and the wing-body junction flow of wall-mounted airfoils (Fleming *et al.* [44], Gand *et al.* [45]).

In the third-octave band of midband frequency 4 kHz (Fig. 11(d)), the tip noise source, located at the corner of the wing tip and the trailing edge dominates the radiation, but weaker trailing edge noise contributions are detected through several isolated noise sources. Similar isolated trailing edge noise sources of a wall-mounted NACA 0012 airfoil on sound maps in $1/12^{th}$ octave band using three-dimensional dipolar beamforming were reported by Porteous *et al.* [20]. The fact that a clear sound source is well located at the wing tip supports the assumption of a dipolar radiation of wing tip noise source, orientated similarly to trailing edge noise (*i.e.*, perpendicularly to the airfoil symmetry axis). Furthermore, the results in Figs. 10 and 11 clearly reveal, interestingly, the tendency of the dominant noise sources turning from leading edge noise and trailing edge noise to wing tip noise at increasing frequency. This is in agreement with the previous experimental results showing the dominant contribution of wing tip noise at high-frequencies (Moreau *et al.* [39], Brooks and Marcolini [46], Geyer *et al.* [40]).

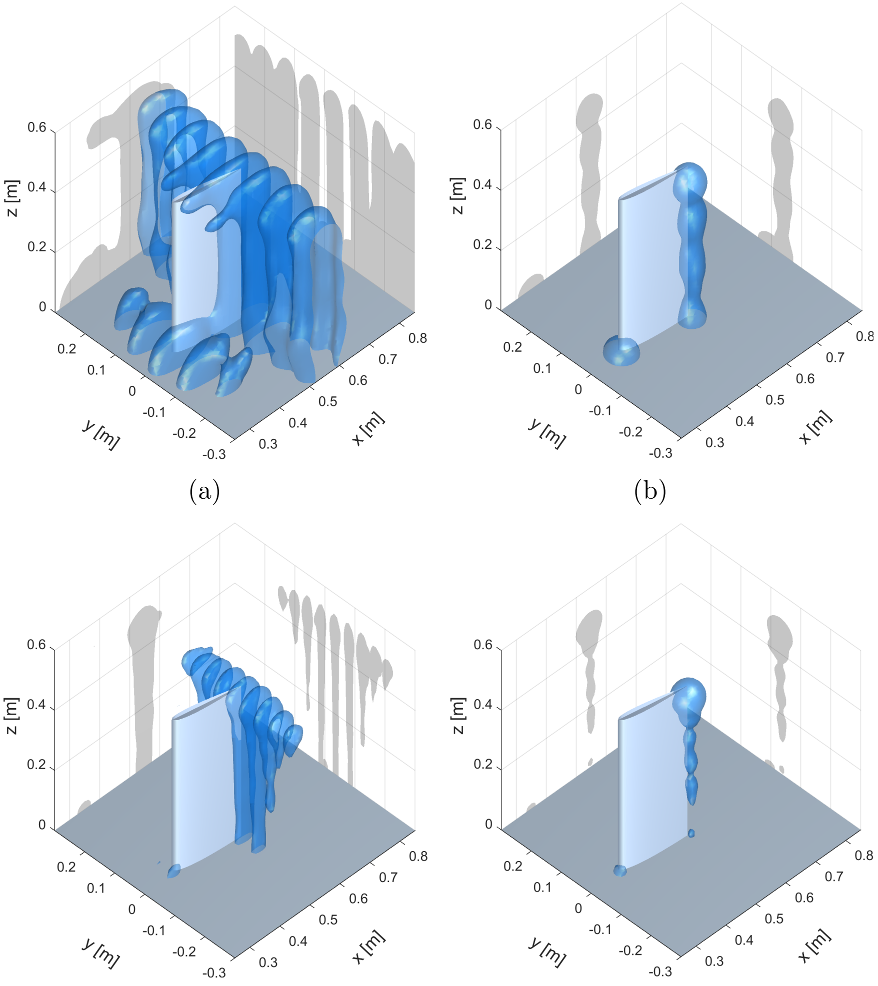

(a) (b)

(c) (d)

Figure 11: Sound maps for the wall-mounted finite airfoil at incoming velocity $U_\infty = 40$ m/s and angle of attack $\alpha = 10°$, at two third-octave bands of nominal midband frequency 2.5 kHz (top figures) and 4 kHz (bottom figures). (a) and (c): 3D dipolar beamforming with respectively a maximum value of 35.2 dB and 30.2 dB on the sound map; (b) and (d): CLEAN-SC technique with respectively a maximum value of 34.4 dB and 30.2 dB on the sound map. The 3D isosurface in each sound map is plotted at 9 dB below the maximum value of the sound map.

Fig. 12 plots the sound maps of the wall-mounted finite airfoil at angle of attack $\alpha = 20°$. In this case, the beamforming result in Fig. 12(a) still shows a main lobe with several side lobes presenting almost the same size. The wing tip noise source is unambiguously identified by using the 3D CLEAN-SC technique (Fig. 12(b)). Similarly, it was reported that wing tip noise dominates the radiation for a wall-mounted NACA 0012 airfoils at angle of attack of 20° (Geyer *et al.* [40]). From the observation of Figs. 10(b), 11(b) and 12(b), it can be concluded that wing tip noise becomes increasingly dominant with increasing angle of attack. The same observation was reported by Moreau and Doolan [47].

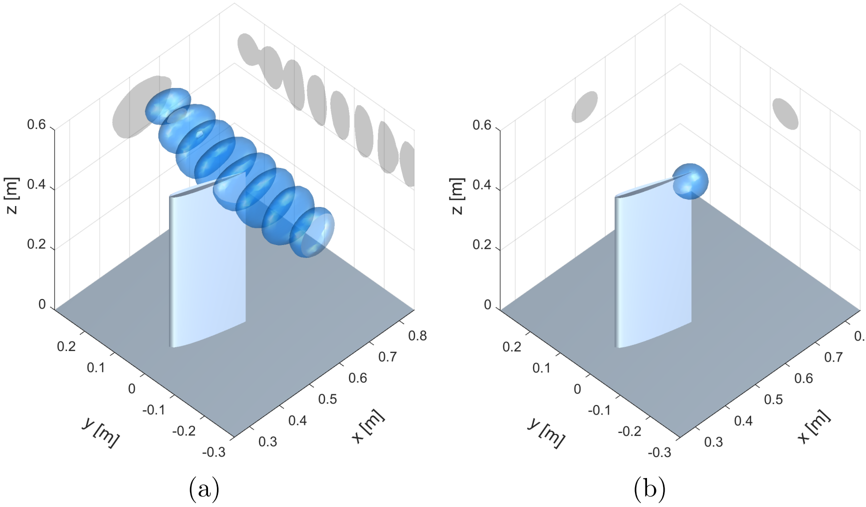

Figure 12: Sound maps for the wall-mounted finite airfoil at incoming velocity $U_\infty = 40$ m/s and angle of attack $\alpha = 20°$, at a third-octave band of nominal midband frequency 2.5 kHz. (a): 3D dipolar beamforming with maximum value of 52.3 dB on the sound map; (b): CLEAN-SC technique with maximum value of 52.2 dB on the sound map. The 3D isosurface in each sound map is plotted at 9 dB below the maximum value of the sound map.

The case of the airfoil at angle of attack $\alpha = 0°$ is now considered, in order to investigate more specifically the lowest and higher frequency bands (midband frequency 0.8 and 5 kHz). Fig. 13(a) presents the beamforming result at low frequency, 0.8 kHz. This range of frequency generates some main and side lobes that have very significant extents, so that the airfoil is totally enclosed in the main lobe, making impossible the identification of the source of noise. Fig. 13(b) shows the sound map after applying the deconvolution by using the CLEAN-SC technique, from which a dominant source concentrated in the middle of the junction and a source concentrated at the trailing edge were identified. Similarly, the dominance of junction noise for a wall-mounted airfoil at low frequencies was reported before (Moreau and Doolan [48]).

Considering the higher frequency band (5 kHz), Fig. 13(c) displays periodic side lobes centered around the leading edge, similarly to Figs. 10 and 11. A difference is however noticeable, with the apparition of lobes at $x = 0.2$ m; these lobes are due to spatial aliasing occurring at high frequencies. Interestingly, the deconvolution process removes the aliasing effect and reveals the existence of the source of trailing edge noise in this frequency band.

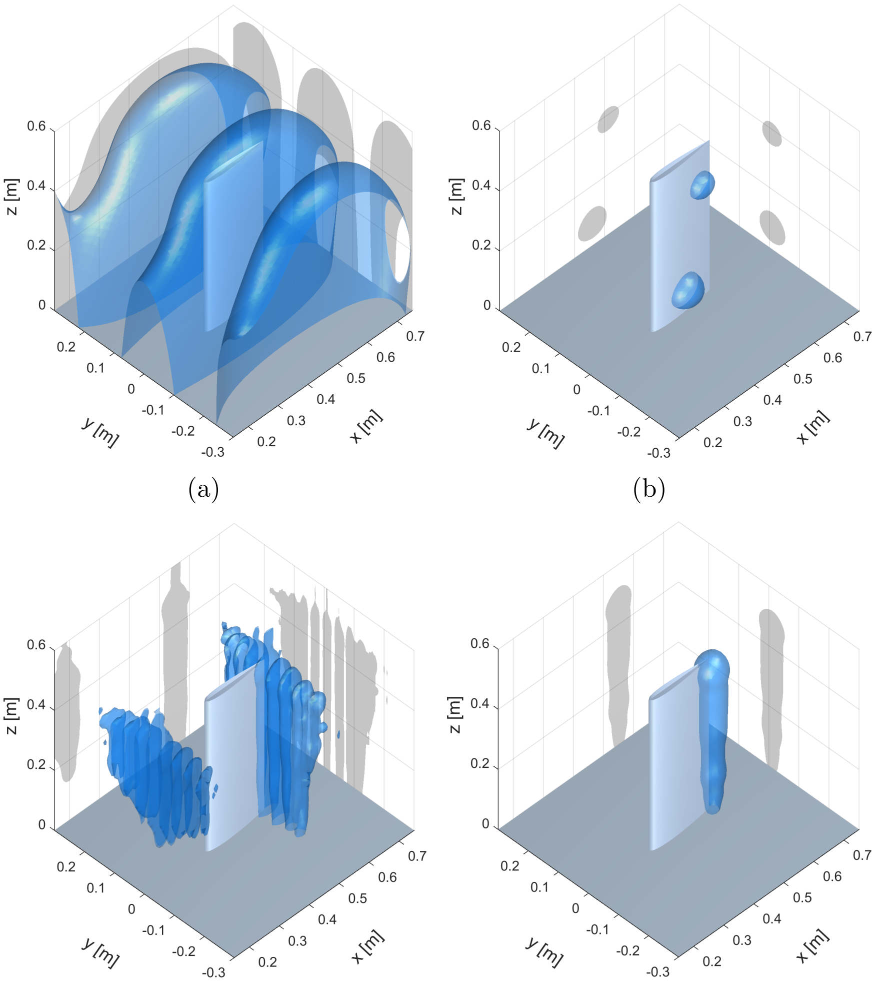

(a) (b)

(c) (d)

Figure 13: Sound maps for the wall-mounted finite airfoil at incoming velocity $U_\infty = 40$ m/s and angle of attack $\alpha = 0°$, at two third-octave bands of nominal midband frequency 0.8 kHz (top figures) and 5 kHz (bottom figures). (a) and (c): 3D dipolar beamforming with respectively a maximum value of 41.9 dB and 35.0 dB on the sound map; (b) and (d): CLEAN-SC technique with respectively a maximum value of 40.8 dB and 35.3 dB on the sound map. The 3D isosurface in each sound map is plotted at 9 dB below the maximum value of the sound map.

4.3. Sound source localization results for two wall-mounted airfoils

To demonstrate the potentiality of 3D array of microphones, a last configuration with two airfoils is investigated. Two wall-mounted airfoils of chord length 0.2 m but with different span lengths (458 mm and 400 mm) and angles of attack of 0° are located in an incoming flow with velocity $U_\infty = 40$ m/s. The leading edge of the shorter airfoil is located 10 cm closer to the wind-tunnel nozzle than the leading edge of the longer airfoil (see Fig. 14). Each airfoil has the same characteristics (apart from the span length) as the airfoil described in Sec. 2.1, with a similar boundary layer tripping device. Hence, the generation of broadband noise is expected in the case. This geometry is a real 3D configuration and cannot be treated by a conventional 2D approach. To investigate the sound produced by this configuration, we used a second array of microphones based on the same technology but with more channels [49]. However, to be consistent with the first experiments, we used only 256 channels among the 1024 available. Fig. 14 shows the array geometry with 16 bars of 16 microphones distributed uniformly (every 72 mm) on each side of the antenna.

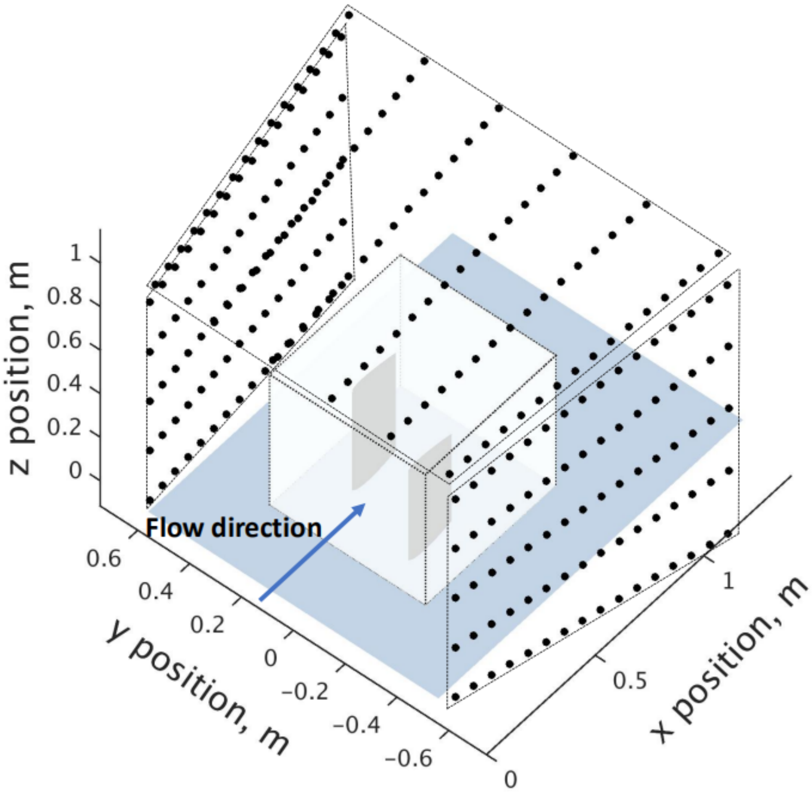

Figure 14: Schematic depicting the 3D microphone array and the two wall-mounted airfoils under study. The black points indicate the positions of the microphones of the 3D microphone array. The cube with dashed edges enclosed by the 3D microphone array shows the 3D scanning grid for the beamforming calculation in a volume of dimension 0.6 m × 0.6 m × 0.6 m.

Fig. 15 yields the sound maps of the two wall-mounted finite airfoils at angles of attack $\alpha = 0^\circ$ and flow speed 40 m/s, in two third-octave bands of midband frequencies 2.5 and 4 kHz. It is found that the overlap of the main lobes and side lobes from the two airfoils makes the beamforming results without deconvolution impossible to interpret (see Fig. 15(a) and 15(c)). Fig. 15(b) and 15(d) show clearly the trailing edge noise sources of the two airfoils using the CLEAN-SC method. The dominant noise source of the short airfoil is more concentrated in the part of the trailing edge close to the tip than that of the long airfoil. In Fig. 15(d), a part of the noise sources was not identified exactly at the trailing edge of the long airfoil, which may be caused by the contamination of the side lobes from the short airfoil. The methods to avoid it could be the optimization of the array geometry to minimize the side lobes. Note that the distribution of the trailing edge noise sources of the airfoils is not as uniform as that shown in Fig. 10. This may be due mainly to three reasons: (i) the existence of the objects, and in particular their possible mutual diffraction, was not considered in the array signal processing technique; (ii) the two airfoils are shorter than that in Fig. 10; (iii) strong side lobes may cause CLEAN-SC to attribute noise to the wrong airfoil and subtract coherent noise (*i.e.*, actual sources) from the other one. Nevertheless, the large array system can be associated to more advanced signal processing methods to account for the solid boundaries of objects for sound imaging.

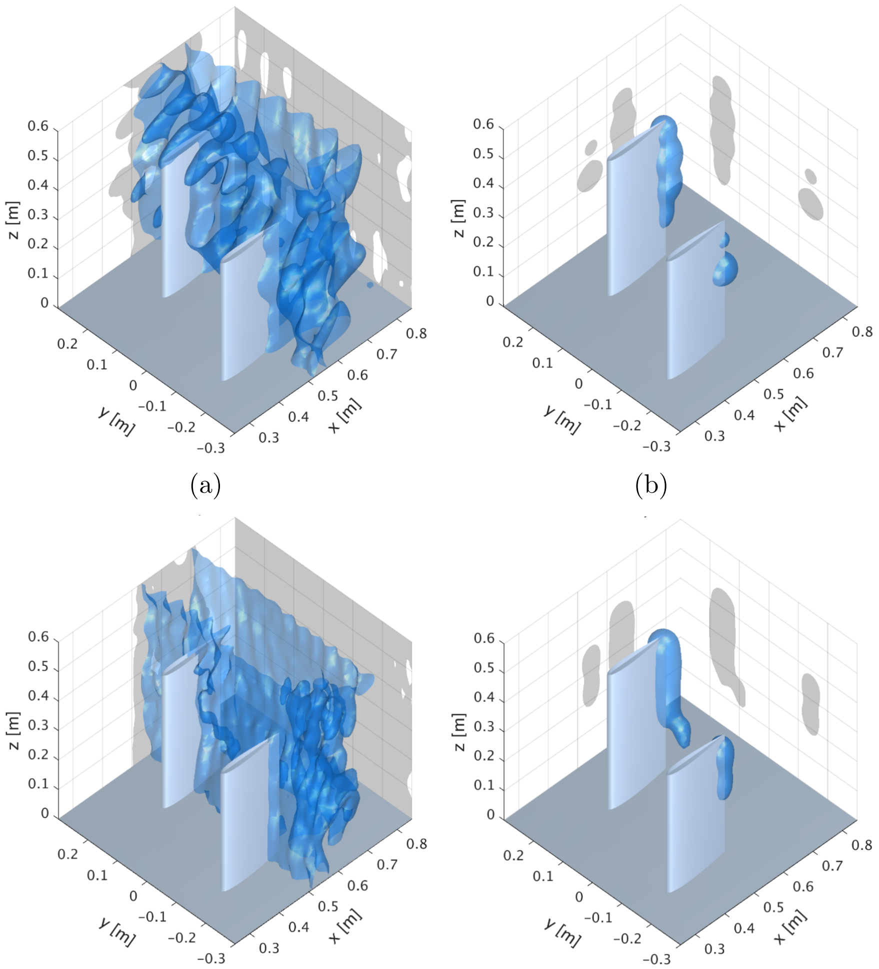

(a) (b)

(c) (d)

Figure 15: Sound maps for the two wall-mounted finite airfoils at incoming velocity $U_\infty =$ 40 m/s and angles of attack $\alpha = 0°$, at two third-octave bands of nominal midband frequency 2.5 kHz (top figures) and 4 kHz (bottom figures). (a) and (c): 3D dipolar beamforming with respectively a maximum value of 41.9 dB and 36.2 dB on the sound map; (b) and (d): CLEAN-SC technique with respectively a maximum value of 40.5 dB and 35.5 dB on the sound map. The 3D isosurface in each sound map is plotted at 9 dB below the maximum value of the sound map.

The results in this study show that the use of a massive 3D array of MEMS microphones, associated to a 3D array processing adapted to dipolar radiation could locate the noise sources of the wall-mounted airfoil in a 3D domain. This 3D beamforming method can reveal accurately the distribution of the noise sources, and is promising for the investigation of the flow-induced noise of objects in flows with a strong 3D configuration. When the existence of the solid boundaries of objects presents some significant influence on the sound propagation in the flow, the calculation of the corresponding Green function could be associated to the beamforming process in future works [50].

5. Conclusion

This paper has presented the development of a tunnel-shaped array for imaging aeroacoustic sources in the open section of an anechoic wind-tunnel, together with the associated signal processing techniques, and an application to the case of a wall-mounted airfoil. The antenna is made of three perpendicular planar arrays enclosing the test section, the lower part of the flow being bounded by a rigid planar surface. The 256 digital MEMS microphones of the 3D array are mounted on 32 bars surrounding the test section of the wind-tunnel, uniformly distributed on each bar. The source under consideration is a wall-mounted NACA 0012 airfoil located in the wind-tunnel flow, for several angles of incidence ranging from 0° to 20°. Such a configuration results in a complex superimposition of several broadband sources of noise, the main source being the trailing edge noise, but also the tip noise, the leading edge noise and the junction noise. A test case concerning two wall-mounted airfoils with different span lengths in a flow using a similar large array system was also addressed.

The data processing is based on a 3D implementation of the beamforming technique associated to a deconvolution method (CLEAN-SC) developed in 3D in order to remove the numerous side lobes that make the interpretation of the sound maps ambiguous. The wall-mounted airfoil being known to generate dipolar sources, the beamforming technique is implemented by using a dipolar radiation model perpendicular to the airfoil. The simulations indicate that the data processing technique allows to identify a linear distribution of non coherent dipoles, similar to the radiation that should be expected from the trailing edge. The flow effect on propagation is taken into account in the beamforming technique by using the Amiet's method in terms of angle correction.

In spite of the relatively low metrological qualities of the MEMS microphones used in this experimental study (compared to measurement microphones), in particular in terms of variability of the amplitude and phase response, the performances of the 3D source localization method are excellent, due to the high number of microphones and to the tunnel-type geometry allowing to surround the sources in the flow. For the wall-mounted airfoil, the different sources of noise that are to be expected are accurately identified in the third-octave bands under investigation, and are in good agreement with experimental results published in the literature. To our knowledge, no 3D beamforming identification of aeroacoustic sources with such level of accuracy have been published formerly in the literature. The presented results prove that a tunnel-type array including several hundreds of microphones associated to appropriate 3D array processing techniques performs very well, and that cheap MEMS microphones are good candidates for measuring the sound radiation efficiently. In the future, the 3D signal processing should be further developed in order to take into account sources with non-constant orientation of the dipole, installation effects such as reflection or diffraction, and non-stationary acoustic events such as in Ref. [51]. Additionally, the large array system can be associated to more advanced array signal processing methods like the time-reversal technique for experimental aeroacoustic investigations.

Acknowledgements

This work is supported by Agence Nationale de la Recherche (ANR), the CPER FEDER project of Région Nouvelle Aquitaine, the Civil Aviation University of China and the China Scholarship Council. The authors wish to thank Pascal Biais, Dominique Busquet, P. Challande, Janick Laumonier, H. Moingeon, Christian Ollivon, Laurent Philippon, Philippe Szeger and Jean-Christophe Vergez for their technical support to this work.

References

[1] Environmental protection-annex 16 to the convention on international civil aviation volume i-aircraft noise, eighth edition, in: International

Standards and Recommended Practices, INTERNATIONAL CIVIL AVIATION ORGANIZATION, 2017.

[2] S. Oerlemans, L. Broersma, P. Sijtsma, Quantification of airframe noise using microphone arrays in open and closed wind tunnels, International Journal of Aeroacoustics 6 (4) (2007) 309–333.

[3] M. Wang, J. B. Freund, S. K. Lele, Computational prediction of flow-generated sound, Annu. Rev. Fluid Mech. 38 (2006) 483–512.

[4] D. H. Johnson, D. E. Dudgeon, Array signal processing: concepts and techniques, PTR Prentice Hall Englewood Cliffs, 1993.

[5] C. S. Allen, W. K. Blake, R. P. Dougherty, D. Lynch, P. T. Soderman, J. R. Underbrink, T. J. Mueller, Aeroacoustic measurements, Springer Science & Business Media, 2002.

[6] H. Siller, M. Drescher, G. Saueressig, R. Lange, Fly-over source localisation on a boeing 747-400, in: Berlin Beamforming Conference (BeBeC), sn, 2010, p. 3.

[7] V. Fleury, J. Bulté, Extension of deconvolution algorithms for the mapping of moving acoustic sources, The Journal of the Acoustical Society of America 129 (3) (2011) 1417–1428.

[8] J. Zhang, X. Xiao, D. Wang, Y. Yang, J. Fan, Source contribution analysis for exterior noise of a high-speed train: Experiments and simulations, Shock and Vibration 2018 (2018).

[9] T. F. Brooks, W. M. Humphreys, A deconvolution approach for the mapping of acoustic sources (damas) determined from phased microphone arrays, Journal of Sound and Vibration 294 (4) (2006) 856–879.

[10] P. Sijtsma, Clean based on spatial source coherence, International journal of aeroacoustics 6 (4) (2007) 357–374.

[11] T. Brooks, W. Humphreys, Three-dimensional applications of damas methodology for aeroacoustic noise source definition, in: 11th AIAA/CEAS Aeroacoustics Conference, 2005, p. 2960.

[12] E. Sarradj, Three-dimensional acoustic source mapping with different beamforming steering vector formulations, Advances in Acoustics and Vibration 2012, article ID: 292695, http://dx.doi.org/10.1155/2012/292695. (2012).

[13] T. Geyer, E. Sarradj, J. Giesler, Application of a beamforming technique to the measurement of airfoil leading edge noise, Advances in Acoustics and Vibration 2012, article ID: 905461, http://dx.doi.org/10.1155/2012/905461. (2012).

[14] T. Padois, O. Robin, A. Berry, 3d source localization in a closed windtunnel using microphone arrays, in: 19th AIAA/CEAS Aeroacoustics Conference, 2013, p. 2213.

[15] A. Mimani, Z. Prime, D. Moreau, C. Doolan, An experimental appli-

cation of aeroacoustic time-reversal to the aeolian tone, The Journal of the Acoustical Society of America 139 (2) (2016) 740–763.

[16] D. Döbler, J. Ocker, C. Puhle, On 3d-beamforming in the wind tunnel, in: Proceedings of the 2016 Berlin Beamforming Conference, Berlin, Germany, 2016.

[17] T. Padois, A. Berry, Two and three-dimensional sound source localization with beamforming and several deconvolution techniques, Acta Acustica united with Acustica 103 (3) (2017) 392–400.

[18] Y. Liu, A. R. Quayle, A. P. Dowling, P. Sijtsma, Beamforming correction for dipole measurement using two-dimensional microphone arrays, The Journal of the Acoustical Society of America 124 (1) (2008) 182–191.

[19] D. J. Moreau, Z. Prime, R. Porteous, C. J. Doolan, V. Valeau, Flow-induced noise of a wall-mounted finite airfoil at low-to-moderate reynolds number, Journal of Sound and Vibration 333 (25) (2014) 6924–6941.

[20] R. Porteous, Z. Prime, C. J. Doolan, D. J. Moreau, V. Valeau, Three-dimensional beamforming of dipolar aeroacoustic sources, Journal of Sound and Vibration 355 (2015) 117–134.

[21] D. P. Arnold, T. Nishida, L. N. Cattafesta, M. Sheplak, A directional acoustic array using silicon micromachined piezoresistive microphones,

The Journal of the Acoustical Society of America 113 (1) (2003) 289–298.

[22] W. Humphreys, Q. Shams, S. Graves, B. Sealey, S. Bartram, T. Comeaux, Application of mems microphone array technology to airframe noise measurements, in: 11th AIAA/CEAS Aeroacoustics Conference, 2005, p. 3004.

[23] S. Pröbsting, F. Scarano, S. Morris, Regimes of tonal noise on an airfoil at moderate reynolds number, Journal of Fluid Mechanics 780 (2015) 407–438.

[24] R. W. Paterson, P. G. Vogt, M. R. Fink, C. L. Munch, Vortex noise of isolated airfoils, Journal of Aircraft 10 (5) (1973) 296–302.

[25] P. Migliore, S. Oerlemans, Wind tunnel aeroacoustic tests of six airfoils for use on small wind turbines, Journal of Solar Energy Engineering 126 (4) (2004) 974–985.

[26] C. Vanwynsberghe, R. Marchiano, F. Ollivier, P. Challande, H. Moingeon, J. Marchal, Design and implementation of a multi-octave-band audio camera for realtime diagnosis, Applied Acoustics 89 (2015) 281–287.

[27] N. Ono, H. Kohno, N. Ito, S. Sagayama, Blind alignment of asynchronously recorded signals for distributed microphone array, in: 2009

IEEE Workshop on Applications of Signal Processing to Audio and Acoustics, IEEE, 2009, pp. 161–164.

[28] C. Vanwynsberghe, P. Challande, F. Ollivier, J. Marchal, R. Marchiano, Geometric calibration of very large microphone arrays in mismatched free field, The Journal of the Acoustical Society of America 145 (1) (2019) 215–227.

[29] R. Amiet, Refraction of sound by a shear layer, Journal of Sound and Vibration 58 (4) (1978) 467–482.

[30] L. Koop, K. Ehrenfried, S. Kroeber, Investigation of the systematic phase mismatch in microphone-array analysis, in: 11th AIAA/CEAS Aeroacoustics Conference, 2005, p. 2962.

[31] M. Howe, The influence of solid boundaries upon aerodynamic sound, Proceedings of the Royal Society of London. Series A, Mathematical and Physical Sciences 231 (1955) 505–514.

[32] C. J. Bahr, L. N. Cattafesta, Wavenumber–frequency deconvolution of aeroacoustic microphone phased array data of arbitrary coherence, Journal of Sound and Vibration 382 (2016) 13–42.

[33] D. Cassereau, M. Fink, Time-reversal of ultrasonic fields-part iii : Theory of the closed time-reversal cavitv, IEEE Trans. Ultrason., Ferroelec., Freq 5.

[34] C. Bahr, N. S. Zawodny, T. Yardibi, F. Liu, D. Wetzel, B. Bertolucci, L. Cattafesta, Shear layer time-delay correction using a non-intrusive acoustic point source., International Journal of Aeroacoustics 20 (2011) 497–530.

[35] T. Padois, C. Prax, V. Valeau, Numerical validation of shear flow corrections for beamforming acoustic source localisation in open wind-tunnels, Applied Acoustics 74 (4) (2013) 591–601.

[36] C. Bahr, N. S. Zawodny, T. Yardibi, F. Liu, D. Wetzel, B. Bertolucci, L. Cattafesta, Shear layer time-delay correction using a non-intrusive acoustic point source, International Journal of Aeroacoustics 10 (5-6) (2011) 497–530.

[37] J. Gershfeld, Leading edge noise from thick foils in turbulent flows, The Journal of the Acoustical Society of America 116 (3) (2004) 1416–1426.

[38] T. F. Brooks, D. S. Pope, M. A. Marcolini, Airfoil self-noise and prediction, Tech. Rep. 1218 NASA Reference Publication (1989).

[39] D. J. Moreau, C. J. Doolan, W. N. Alexander, T. W. Meyers, W. J. Devenport, Wall-mounted finite airfoil-noise production and prediction, AIAA Journal (2016) 1637–1651.

[40] T. F. Geyer, D. Moreau, J. Giesler, P. Hall, E. Sarradj, C. J. Doolan, Measurement of the noise generated by wall-mounted airfoils of different

thickness, in: 2018 AIAA/CEAS Aeroacoustics Conference, 2018, p. 3796.

[41] A. Uzun, M. Y. Hussaini, Simulations of vortex formation around a blunt wing tip, AIAA Journal 48 (6) (2010) 1221–1234.

[42] T. Imamura, S. Enomoto, H. Kato, Y. Yokokawa, K. Yamamoto, Numerical simulation of naca0012 wingtip flow leading to noise generation, in: 11th AIAA/CEAS Aeroacoustics Conference, 2005, p. 2864.

[43] S. C. Bailey, S. Tavoularis, B. H. Lee, Effects of free-stream turbulence on wing-tip vortex formation and near field, Journal of aircraft 43 (5) (2006) 1282–1291.

[44] J. Fleming, R. Simpson, J. Cowling, W. Devenport, An experimental study of a turbulent wing-body junction and wake flow, Experiments in Fluids 14 (5) (1993) 366–378.

[45] F. Gand, V. Brunet, S. Deck, Experimental and numerical investigation of a wing-body junction flow, AIAA journal 50 (12) (2012) 2711–2719.

[46] T. F. Brooks, M. A. Marcolini, Airfoil tip vortex formation noise, AIAA journal 24 (2) (1986) 246–252.

[47] D. J. Moreau, C. J. Doolan, An experimental study of airfoil tip vortex formation noise, in: Proceedings of ACOUSTICS, Brisbane, Australia, 2016.

[48] D. J. Moreau, C. J. Doolan, Tonal noise production from a wall-mounted finite airfoil, Journal of Sound and Vibration 363 (2016) 199–224.

[49] Y. Zhou, F. Ollivier, P. Challande, R. Marchiano, V. Valeau, D. Marx, C. Prax, Design and use of a three-dimensional array of mems microphones for aeroacoustic measurements in wind-tunnels, in: Berlin Beamforming Conference (BeBeC, Berlin), 2020.

[50] S. Bousabaa, J. Bulté, D.-C. Mincu, R. Marchiano, F. Ollivier, Sparse green's functions estimation using orthogonal matching pursuit: Application to aeroacoustic beamforming, AIAA Journal 56 (6) (2018) 2252–2270.

[51] J. Fischer, V. Valeau, L.-E. Brizzi, Beamforming of aeroacoustic sources in the time domain: an investigation of the intermittency of the noise radiated by a forward-facing step, J. Sound Vib. 383 (2016) 464–485.